

Effective Angle of Attack Measurements in Active Control for Vortex Gust Mitigation

Efe Egemen Sen*, Murat Saritas†, Oksan Cetiner‡,
Istanbul Technical University, Istanbul 34469, Turkey

Murat Bronz§
ENAC, University of Toulouse, F-31055 Toulouse, France

Gust encounters can have adverse effects on the flight stability and trajectory of air vehicles. These effects are particularly pronounced for Micro Air Vehicles (MAVs) which generally fly at velocities of the same order of magnitude with the flow velocity changes induced by atmospheric gusts. This study proposes and experimentally demonstrates the use of effective angle of attack measurements taken from upstream of a NACA0012 wing that is exposed to a continuous vortex gust generated by the wake of an upstream cylinder for the mitigation of gust-induced loads by feed-forwarding the measurements to actuate a trailing edge flap to exploit the temporal gap between the measurement and the force development in the air. Follow-up water channel experiments have been performed to verify the validity of the measurements performed in the air. It was seen that feed-forwarding the angle of attack measurements in water fails due to the added mass effects present in the medium. An ODE solution was implemented to work around the issue and, through a few iterations, a force mitigation of 74.40% was achieved.

I. Introduction

As the integration of unmanned aerial systems to the urban airspace continues, achieving stabilized flight through these highly unsteady aerodynamic environments still poses a great challenge [1, 2]. Since their flight velocities are in the same order of magnitude as the velocity transients caused by the wake of tall structures, flights of micro air vehicles (MAVs) are especially susceptible to these disturbances [3]. A considerable amount of work is present in the literature characterizing the aerodynamic behavior of rigid wings upon gust encounters. An overview of the current state-of-the-art is provided and canonical gust encounter types are addressed by Jones et al. [4]. These canonical gust encounters are studied in three categories: streamwise gusts, transverse gusts, and vortex gusts as can be seen in Figure 1 [5]. All of these gust types severely affect the handling qualities of aircraft, which necessitates a mitigation strategy. Among the studied mitigation strategies for each category of gust, Chowdhury and Ringuette [6] used a rotating wingtip to alleviate the loads of a streamwise gust and obtained considerable results. Angulo and Babinsky [7, 8] controlled the pitch angle of a wing to mitigate a transverse gust with three different pitching profiles and achieved mitigation of as much as 95% relative to the uncontrolled response. Acar [9] showed the presence of a strong correlation between ΔC_L and the effective angle of attack measurements obtained from DPIV imaging for a vortex gust and computationally recreated the flow conditions.

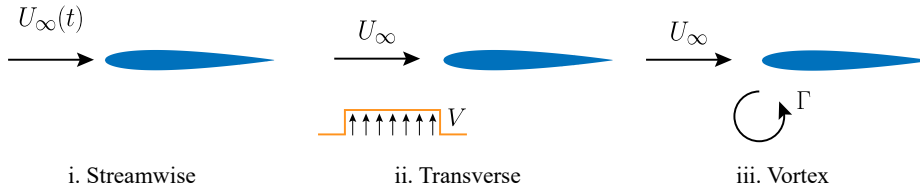


Fig. 1 Canonical gust types as defined by [5].

*B.Sc. Student, Department of Astronautical Engineering, ITU.

†Ph.D. Student, Department of Aeronautical Engineering, ITU.

‡Professor, Department of Astronautical Engineering, ITU, AIAA Associate Fellow.

§Assistant Professor, ENAC Lab - OPTIM - Dynamic Systems, murat.bronz@enac.fr, AIAA Member.

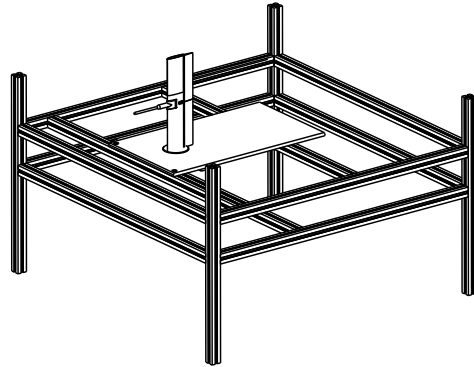
The main objective of this study is to attempt to mitigate the effects of continuous vortex gust structures produced by a circular cylinder on a NACA0012 wing, which has been selected due to its wide use in the literature, with the use of effective angle of attack measurements that come from a multi-hole pitot probe that has been placed upstream of the wing. The wing incorporates a trailing edge flap to control the forces. Due to the involved time scales and flow visualization difficulties, most of the vortex gust experiments have been performed in water channels or towing tanks at relatively low free stream velocities [10–12]. Another aim of this study is to fill the existing gap for wind tunnel-based experiments and take gust mitigation experimentation one step closer to airborne flight tests on MAVs. In addition to the wind tunnel experiments, a number of follow-up experiments in a water channel have been performed at the Trisonic Laboratory of the Faculty of Aeronautics and Astronautics of Istanbul Technical University. Taking real-time angle of attack measurements in the water channel is challenging. Therefore, upon ensuring the repeatability of the experiments, time-resolved digital particle image velocimetry data has been used to acquire the time distribution of the angle of attack signal. Using this information, an ordinary differential equation has been used to model the time variation of the coefficient of lift.

II. Experimental Setups

The wind tunnel experiments have been conducted inside the indoor flight arena of Ecole Nationale de l'Aviation Civile in Toulouse where the free-stream flow has been generated by a WindShape which is a multi-fan wind generator, an alternative to a wind tunnel for lower-fidelity applications. It consists of modules of fan arrays that are controlled by the onboard computer which communicates with the peripheral hardware through a network connection. For this application, a 1.5 x 0.75 m WindShape has been used. A flow filter is placed in front of the device that lowers the turbulence intensity. Cylinders of various diameters have been used to generate a continuous vortex gust field. In order to adjust the frequency of vortex shedding, the diameter of the cylinders has been theoretically calculated using the Strouhal number relation. The results presented are for an upstream cylinder of 30 cm diameter. Fig. 2 shows the experimental facility and the sketch for the setup.



(a) Experimental facility.



(b) Sketch for the setup.

Fig. 2 The experimental facility and the sketch for the setup.

A NACA0012 wing has been designed and manufactured out of PLA using 3D printers. The wing has a chord of 150 mm and a semi-span of 470 mm, resulting in an effective aspect ratio of 6.3, eliminating the 3D flow effects [13]. The flap is 0.4 chords in length, as a consequence of the trade-off made between flap effectiveness and real-life applicability. The flap actuator servo is MKS HV93. Compared to conventional servos that use a 50 Hz PWM signal for modulating the position command, this servo uses a non-standard 560 Hz PWM signal with a center position of $760 \mu s$, hence, greatly increasing the bandwidth of the control system. In order to keep the flow relatively clean, the servo actuates the flap through a spur gear. The internal routing also enables the cabling to be out of the flow. For the CAD design, Dassault Systèmes CATIA has been used, while IdeaMaker slicer software has been used to generate the g-codes for the 3D printers. The flap actuator MKS HV93 does not incorporate a dedicated position feedback signal that can be outputted without modifying its structure, hence, a US Digital MA3-A10-125-B encoder, with a resolution of 10 bits, has been fitted on the surface of the wing to quantify the reference tracking performance of the servo.

The wing mount mechanism consists of two steel tubes fitted to a steel endplate with an axial hole for cable routing. This whole assembly is directly connected to the force/torque sensor which itself is connected to a clutch mechanism. The clutch mechanism is connected to the HEBI X5 robotic actuator that controls the pitch angle of the whole assembly. In case a free-to-rotate model is required, this clutch can be disengaged. In this case, however, the robotic actuator has been used to calibrate the 0° angle of attack position and hold it. The data acquisition board (DAQ) used for the project is LabJack T7. This DAQ board communicates with the experiment computer through the network, enabling the whole experiment to be run from a single script. ATI Mini40 has been used as the force/torque sensor due to its suitability for the expected range of loads and its availability. The sensor is powered through ATI 9105-PS-1 power supply which also conditions the signal before sending it to LabJack. The multi-hole probe used to measure airspeed and angle of attack is an in-house product developed at ENAC [14]. It consists of an STM32F7 microcontroller, 3 SDP31 differential pressure sensors, and an LPS33HW absolute pressure sensor in a 22 mm diameter carbon fiber tube casing and communicates with the experiment computer over a USB connection.

The water channel experiments have been conducted in the large-scale free-surface water channel located in the Trisonic Laboratory of Istanbul Technical University. The vortex gust is generated by one-half of a clockwise rotation of a gust generator plate about its midchord. The gust generator plate used for the experiments is a 10 cm x 40 cm acrylic flat plate with a wedge-shaped leading edge and trailing edge. The free surface acts as a symmetry plane, therefore the gust generator has an effective aspect ratio of eight. The motion of the gust generator lasts for four convective times and a (negative) vortex gust is formed with a trajectory aligned with the chord line of the model. A LabJack T7 is used to obtain the force/torque data from an ATI Nano 25 F/T sensor while simultaneously controlling a Savöx SW-1250MG servo which actuates the 50% chord flap mounted on a 10 cm x 20 cm flat plate wing model.

The digital particle image velocimetry (DPIV) system uses a dual cavity Nd:YAG laser of producing 120 mJ/pulse maximum energy to illuminate the flow which is seeded by polyamide particles of $20 \mu\text{m}$ average diameter. Images are captured at 10Hz with a CCD camera having 10-bit depth and 1600×200 pixels resolution, attached to Nikon objectives of 60 mm focal length. The camera is positioned beneath the channel perpendicular to the plane of investigation. The captured images are cross-correlated using Adaptive PIV algorithm of Dantec Dynamic Studio V4.10.67. The experiments for each case are repeated for 5 times and finally ensemble-averaged. The details of the experimental setup and the gust characterization can be found in [15]. On the other hand, the vortex gust effects on the loading and corresponding flowfield measurements are given in [12] in comparison with a transverse gust case.

III. Results

A. Force Data Validation

The aluminum test rig that has been used to mount the sensor assembly is free to move with wheels to facilitate running different experiments in front of the WindShape. This mobility comes with the cost of not having a fixed reference to adjust the attitude of the model relative to the flow. However, using the high angular resolution (0.005°) of the pitch angle control actuator HEBI X5's position feedback, it is possible to accurately control and measure the attitude of the wing relative to the test rig. Taking advantage of this capability along with the use of a symmetrical airfoil, it has been possible to pinpoint the zero angle of attack attitude by performing an angle of attack sweep with a pitch rate low enough to prevent unsteady effects from becoming important.

An initial sanity check for the force sensor readings has been performed by weighing known masses in all three axes. After this validation, the pitch angle control actuator was commanded from -20° to $+20^\circ$ in 60 seconds with respect to an arbitrary reference position determined by crudely aligning the wing to the expected flow direction. The force data obtained from this sweep motion was filtered with a low-pass Butterworth filter at a cut-off frequency of 3 Hz. Using this data, due to the symmetrical geometry of NACA0012, the angular position corresponding to the lowest resultant aerodynamic force is used to update the reference angular position and the same experiment is repeated with a narrower sweeping range until the range becomes small enough to not give repeatable results due to noise which corresponds to a range of approximately $\pm 0.2^\circ$.

After calibrating the angle of attack control, a similar angle of attack sweep was performed again, this time with the intention of validating the aerodynamic force coefficients of the wing. For this step, a Trotec TC 100 thermohygrometer

was used to determine the density value for the calculation of dynamic pressure. The following transformation was used to calculate the lift and drag.

$$\begin{bmatrix} L \\ D \end{bmatrix} = \begin{bmatrix} -\sin(\alpha) & \cos(\alpha) \\ \cos(\alpha) & \sin(\alpha) \end{bmatrix} \begin{bmatrix} F_T \\ F_N \end{bmatrix}$$

The resultant aerodynamic force with respect to the angle of attack obtained during this experiment can be seen in Fig. 3a. Additionally, Fig. 3b presents the data obtained for the lift coefficient with $C_{L,max} \approx 0.8$ occurring at $\alpha = 14.1^\circ$. Furthermore, an asymmetrical behavior for the negative angle of attack can be observed since the flow starts with a stalled wing, thus, stall hysteresis shows its effects.

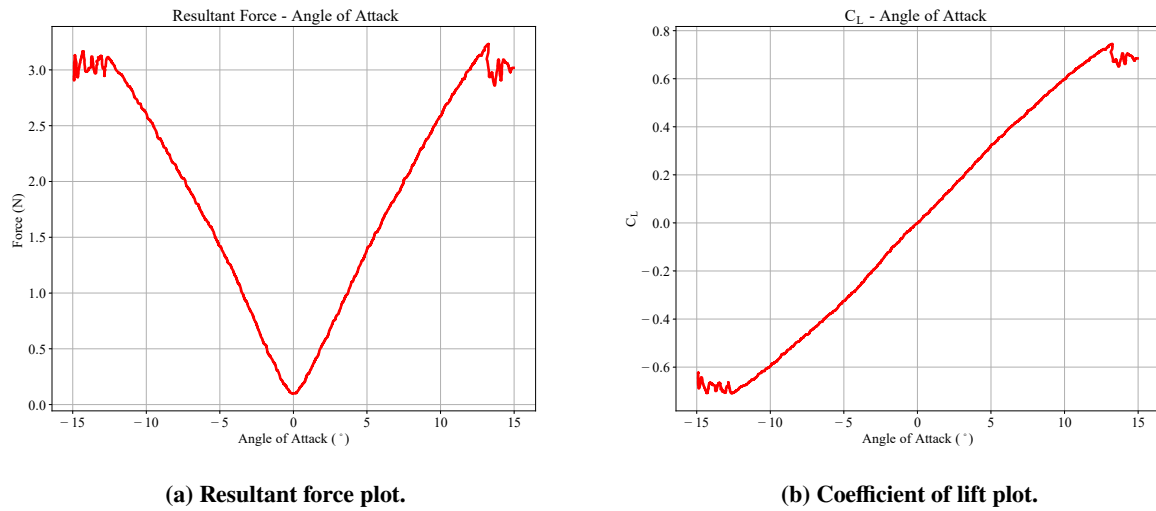


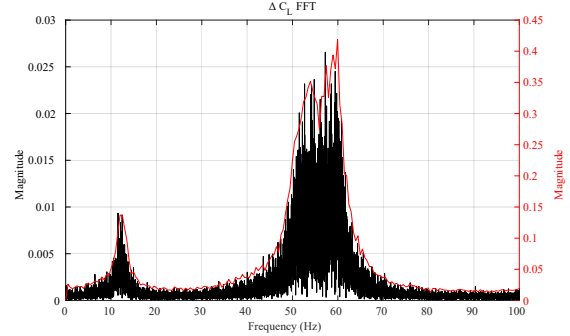
Fig. 3 Data obtained during force validation.

B. Vortex Gust Interaction Characterization

Initially, a cylinder with a diameter of 3.75 cm (Fig. 4a) has been selected to make use of the existing experimental data from Babu et al. [16] by keeping the chord-to-diameter ratio equal to 4 and positioning the wing 8 diameters downstream of the cylinder. The free-stream speed has been calculated to be 2.42 m/s based on matching the Reynolds number of 7500 for the cylinder. However, initial crude data acquisitions showed that it is impossible to obtain a meaningful signal-to-noise ratio on the force measurements at this free-stream velocity. Therefore, the velocity has been increased to 10.5 m/s for the characterization phase. Using the Strouhal number relation, $St = fD/U_\infty = 0.2$ the expected vortex shedding frequency is approximately 56 Hz. In terms of amplitude, the aim is to match the effect of a large-scale continuous vortex gust encounter on the lift as obtained in controlled experiments performed in water by Soy et al. [17] and it seems this is accomplished at least in orders of magnitude based on the frequency spectrum plotted in red in terms of frequency bins of width 0.5 Hz (see Fig.4b).



(a) Vortex generator cylinder in front of the WindShape.



(b) Fast Fourier transform of the force data.

Fig. 4 The vortex generator and frequency analysis.

Even though the expected frequency for the gust response has been acquired at 53 Hz as seen in Fig. 4b, two additional peaks have been observed at 12 Hz and 60 Hz which later experimentation showed to be the structural modes of the wing. In addition, a frequency sweep has been performed with the servo and it was seen that it is not able to keep up with the frequency of 53 Hz generated by the 3.75-cm cylinder. Therefore, the cylinder was replaced with a 30-cm-diameter one, and the free-stream velocity was reduced to 6.4 m/s, resulting in a vortex shedding frequency of 4.26 Hz, calculated through the Strohal number relation.

The experiments have shown that the presence of structural modes in the force signal is even worse in this configuration. Therefore, a series of tests have been conducted to find a position where the effects of gust can be clearly distinguished from the structural excitation of the wing. The final position that was achieved by meeting these requirements without altering the free-stream velocity; and the new cylinder diameter can be seen in Fig. 5 and the corresponding Fast Fourier transform of the coefficient of lift measurements can be seen in Fig 6a. The first peak occurring at 4.96 Hz corresponds to the vortex shedding frequency and the peaks observed at frequencies greater than 10 Hz are attributed to the structural modes of the wing.

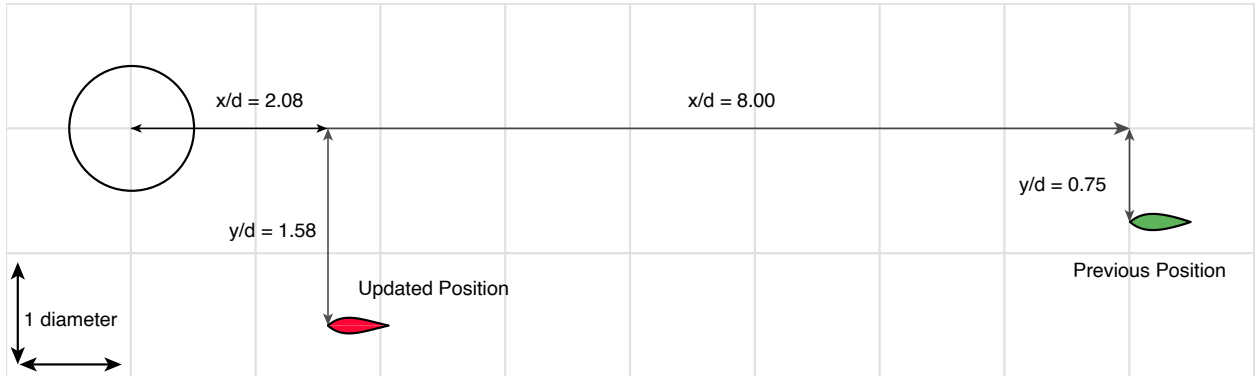


Fig. 5 Large cylinder and the updated position.

Statistical data corresponding to 10 repetitions of lift measurement experiments in this position can be seen on the no control lift coefficient column of Table 1. The mean ΔC_L values obtained in the experiments match with the data obtained by Soy et al. [17] showing that the wing actually encounters a large-scale continuous vortex gust.

C. Effective Angle of Attack Measurements and Mitigation

Originally, mitigation was attempted through force-feedback-based closed-loop control. However, the excitation of the structural modes of the wing under the effects of gusts and the case that force sensor measuring the inertial forces

generated by the flap's motion through the controller's output resulting in a rapid divergent oscillation quickly discarded this method.

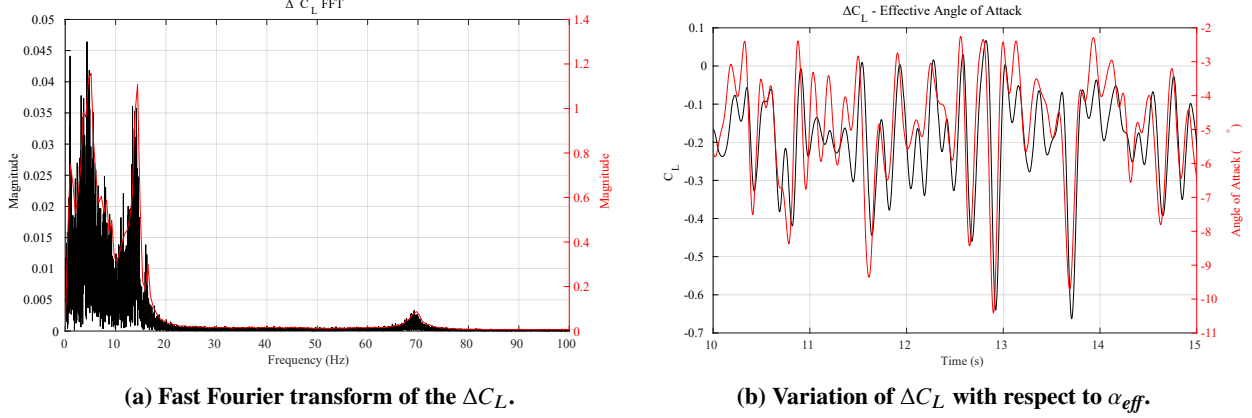


Fig. 6 Data obtained from the large cylinder experiments.

Further experimentation showed that there is a strong correlation between the measured effective angle of attack and lift signals with a 28 ms phase difference as can be seen in Fig. 6b. This phase difference figure also corresponds to the convective time it takes for the free-stream flow velocity to cover the streamwise distance from the pitot tube's entrance to the leading edge of the wing.

In order to exploit this temporal gap between the effective angle of attack measurement and the force development, a feed-forward controller architecture, which takes the measured angle of attack as its input and outputs the flap deflection angle, was adopted. The gain of the controller was tuned with respect to the $C_{L,\delta}$ slope obtained by performing a flap deflection sweep. The data corresponding to the controlled experiments can be seen in Table 1.

Table 1 Comparison of controlled and no control experiments.

Exp. #	No Control Lift Coefficient		Controlled Lift Coefficient		Inertial Forces	
	$\mu, \Delta C_L$	$\sigma, \Delta C_L$	$\mu, \Delta C_L$	$\sigma, \Delta C_L$	$\mu, \Delta C_L$	$\sigma, \Delta C_L$
1	-0.18407	0.13009	0.03626	0.10796	-0.00128	0.12852
2	-0.18542	0.13512	0.04472	0.10123	-0.00035	0.13048
3	-0.18626	0.13129	0.05195	0.10299	-0.00030	0.13277
4	-0.18415	0.13754	0.06647	0.09149	0.00011	0.12523
5	-0.18425	0.13223	0.05269	0.10067	-0.00118	0.13365
6	-0.18494	0.13391	0.03171	0.10355	0.00051	0.13033
7	-0.18305	0.13146	0.03210	0.10742	0.00050	0.13994
8	-0.19958	0.13345	0.02924	0.10412	0.00080	0.11325
9	-0.18472	0.14250	0.04120	0.10460	-0.00183	0.12904
10	-0.18419	0.14230	0.05929	0.09377	0.00083	0.13849
Average	-0.18606	0.13499	0.04456	0.10178	-0.00022	0.13017

Although the controller was able to shift the mean value of the lift coefficient to the vicinity of zero, considering the standard deviation, the fluctuation still exists. The source of this fluctuation was investigated by recording the controller's output and the flap's actual position in order to make sure that the actuator's reference tracking was adequate. Later on, the controller output signal was replayed without a flow and the inertial forces generated by the flap's motion were isolated and it was reasoned that most of the contribution to the fluctuation in the controlled cases are sourced from the inertial forces generated by the flap.

As the experimentation concluded in the air, the second phase began in the water channel. The primary goal of switching to water was to be better able to visualize and characterize the flow field. However, this ability came with the cost of not obtaining real-time angle of attack measurements. To work around this issue, it was shown that the discrete gust produced in the water could be coherently reproduced, hence, the data was used if it were taken in real-time.

D. Discrete Vortex Gust Encounter in Water

The vortex gust in the water channel is created by pitching a flat plate 180 degrees around its mid-chord. This motion creates two vortices, one clear negative vortex, and an early, rather faint, positive vortex. The half-rotation of the gust generator takes 4 seconds to complete. The ensemble-averaged values of the lift force coefficient transient as a result of 5 experiments can be seen in Figure 7.

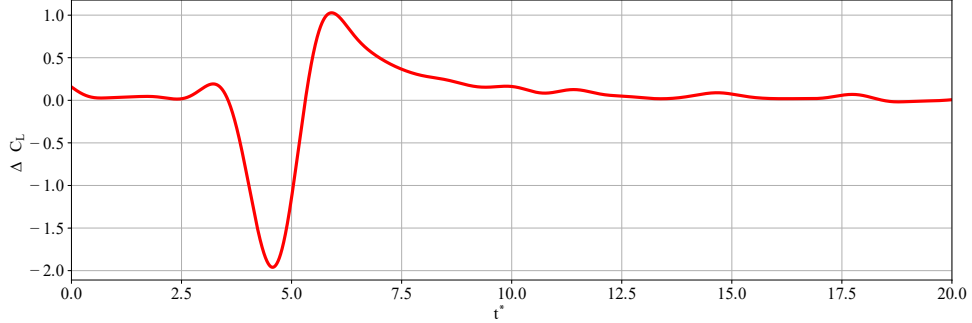


Fig. 7 Coefficient of lift change for a vortex gust encounter trajectory aligned with the chord line.

To be able to compare the results, Acar's [9] main case has been used. This case consists of the gust generator placed 55 mm upstream and 36 mm in the stream-normal direction of the model to obtain a vortex gust encounter trajectory aligned with the chord line. All the experiments take 60 seconds in duration. After the flow settles around $t^* = 20$, the rest of the 40 seconds is averaged and taken as the reference value of the ΔC_L value. The DPIV vector field obtained from these experiments has been used to obtain the angle of attack data which can be seen superimposed to the lift measurements in Figure 8. In accordance with Acar [9], the area of extraction has a vertical and horizontal separation of 2.5 and 20 mm, respectively. The data, which was acquired at 10 Hz, was low-pass filtered and resampled.

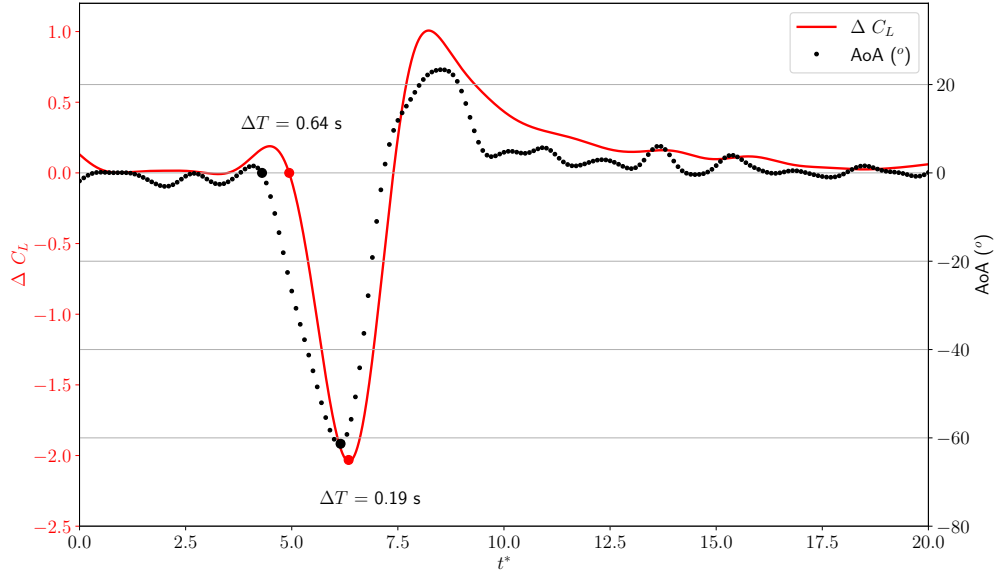


Fig. 8 Angle of attack data for a vortex gust encounter trajectory aligned with the chord line.

The angle of attack signal is highly correlated and leads the force signal with a variable time gap. Since obtaining real-time angle of attack measurements in water is another challenge on its own, the angle of attack data obtained from experiments without control was used with the justification that they can be coherently reproduced in independent experiments. However, when a similar strategy of feed-forwarding the angle of attack measurements to the flap deflection was applied to the water case, no significant mitigation was obtained. The primary reason identified is the added mass effects caused by the mass of the fluid displaced by the flap's motion. In order to work around this phenomenon, a simple ordinary differential equation was set up to model the forces as a function of the flap deflection angle.

Without taking into account the time gap, the steady coefficient of lift due to the angle of attack is modeled as,

$$C_{Lss} = k2\pi\alpha \quad (1)$$

The value for k has been found to be 0.304 from the experimental data. Mitigation of this force requires precise positioning of the flap. When a flap is added to the system, the effective camber line becomes the line connecting the leading edge to the trailing edge. For a 50% chord flap, this corresponds to the relation $\alpha = \delta/2$.

Additionally, during the flap motion, the geometric rotation of the flap induces additional fluid motion, resulting in a virtual camber effect [18, 19]. Modeling the flap as a flat plate being pitched from its leading edge yields the virtual camber contribution as,

$$C_{L_{virtualcamber}} = \frac{\pi(c/2)}{2U_\infty} \dot{\delta} \quad (2)$$

Furthermore, upon flap acceleration, a significant mass of water is displaced. This displacement discloses itself in the form of added mass in the force measurements [18, 19].

$$C_{L_{addedmass}} = \frac{\pi(c/2)^2}{4U_\infty^2} \ddot{\delta} \quad (3)$$

Summing up these contributions in a single equation yields,

$$C_L = k\pi\delta + \frac{\pi(c/2)}{2U_\infty} \dot{\delta} + \frac{\pi(c/2)^2}{4U_\infty^2} \ddot{\delta} \quad (4)$$

Since, from previous measurements, it is known that the angle of attack data correlates well with the force measurements, the time history of C_L is used to solve the above second-order ordinary differential equation. The solution, obtained using MATLAB's ODE45 solver, can be seen in Figure 9 with the validation of the solution can be found in Figure 15 in Appendix A.

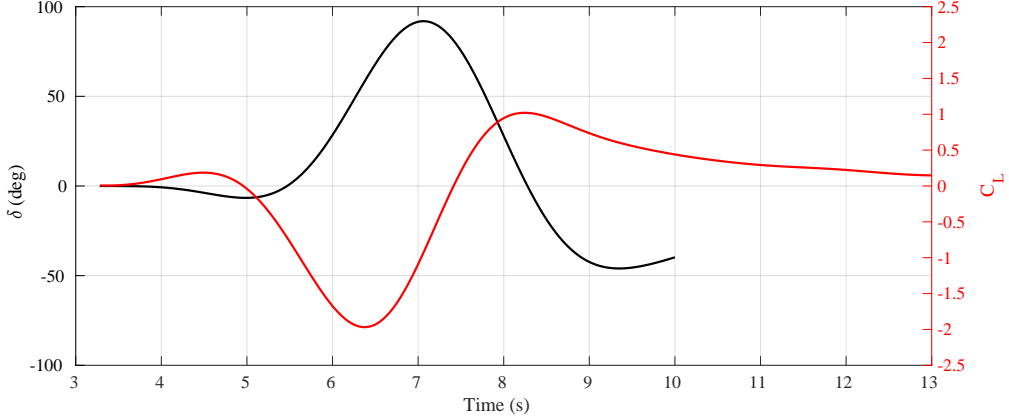


Fig. 9 Flap deflection solution obtained from the ODE.

E. Discrete Vortex Gust Mitigation in Water

The flap motion profile obtained from the solution of the ordinary differential equation has been used in an attempt to mitigate the effects of the vortex gust. However, since the solution contains certain intervals that command more than 45° of flap deflection, which is the mechanical limit of the model, it is clipped to prevent mechanical damage. The ensemble-averaged force data, the commanded flap deflections, and the corresponding angle of attack signal can be seen in Figure 10 below. Additionally, the reference tracking performance of the flap has been tested and the verification can be seen in Figure 17 in Appendix B.

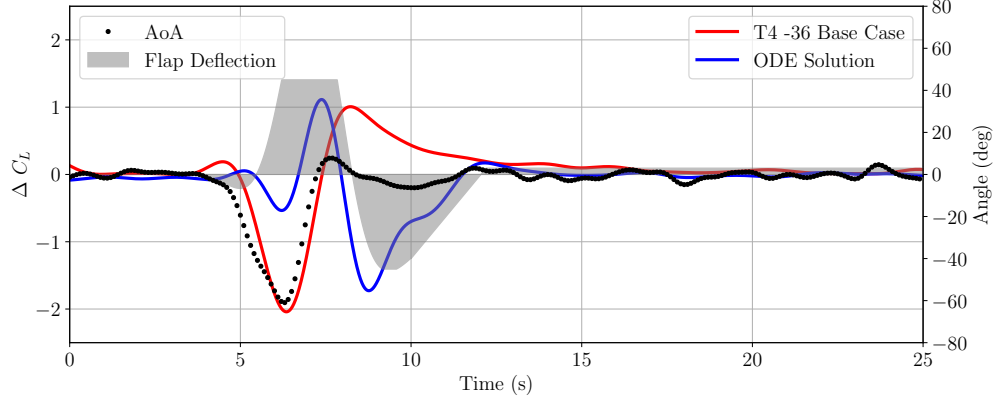


Fig. 10 Mitigation profile using the ODE solution.

It can be seen from the data that although the initial motion of the flap is considerably effective at mitigating both the small disturbance that comes just before the huge negative peak and the huge negative peak itself, the clipped portion of the signal results in a positive peak. Following this peak, the return portion creates a large added mass effect and results in another negative peak just as strong as the one present in the base case. The main reason behind this discrepancy between the experimental results and the ODE solution is the fact that once the flap starts moving, the surrounding flow field no longer matches the conditions of the solution.

To work around these issues, a linear return motion was added to the flap deflection (Figure 11). The start of the return motion was matched with the instant of zero-crossing of the lift force in the previous mitigation attempt. This configuration yielded a much better force behavior by preventing both the initial positive peak due to clipping and the large negative peak due to added mass. Nevertheless, a positive similar to the base case in magnitude is still present.

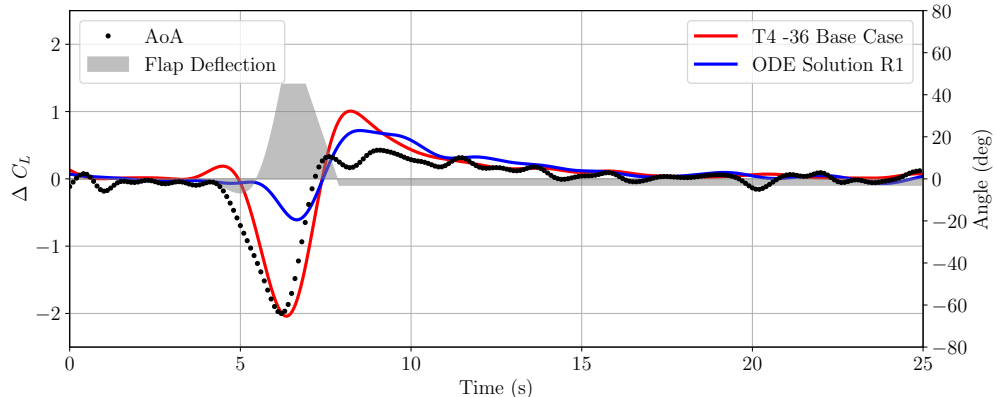


Fig. 11 Mitigation profile using the ODE solution with linear return.

Addressing the secondary positive peak problem was accomplished by reintroducing the negative portion of the flap

deflection profile, as seen in Figure 12. The linear return part was extended to -20° without changing the speed of the flap. This profile yielded the best results, reducing the peak magnitude by 74.4%.

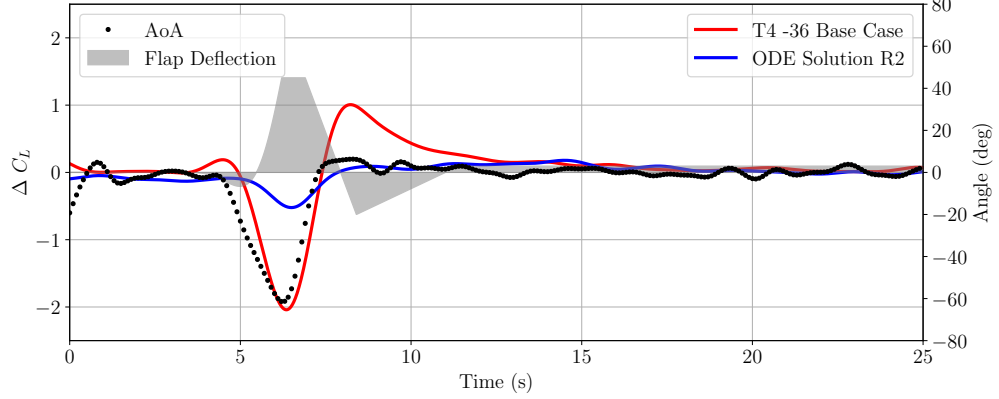


Fig. 12 Mitigation profile using the ODE solution with linear negative position.

In addition to the experiments performed with the basis of the ODE solution, a classical force-feedback PD controller that takes the real-time filtered lift force as its input was tested as well. The tuned parameters of the controller can be seen in Table 2.

Table 2 Feedback control parameters.

Parameter	Value	Unit
P	100	deg/N
D	10	deg/N

The results for the PD controller can be seen in Figure 13. As can be seen from the saw-tooth-like flap deflection, the forces created by the flap's motion again, poses a significant problem. Although heavy filtering was applied to alleviate the effects, doing so introduced temporal delays that impair the system's performance.

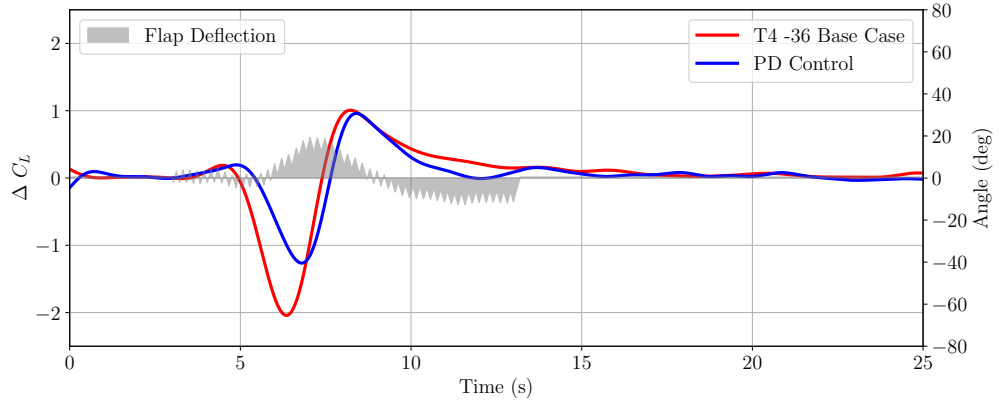


Fig. 13 Mitigation profile using the PD controller.

A summary of the results for the control experiments performed in the water channel is presented in Table 3. Additionally, the DPIV images containing the vorticity distributions of no control and controlled experiments can be seen in Figure 14. The selected instants $t^* = (4.5, 6.3, 7.5)$ correspond to (1) the initial small positive peak, (2) the large negative peak, and (3) the zero-crossing before the large positive peak, respectively.

Table 3 Summary of ODE-based control experiments.

Control Experiment	Negative Peak ΔC_L	% Mitigation	Positive Peak ΔC_L	% Mitigation
PD Controller	-1.265	38.05	0.960	0.4
ODE Solution	-1.728	15.36	1.114	-10.60
ODE Solution R1	-0.609	70.16	0.718	28.65
ODE Solution R2	-0.522	74.40	0.180	82.13

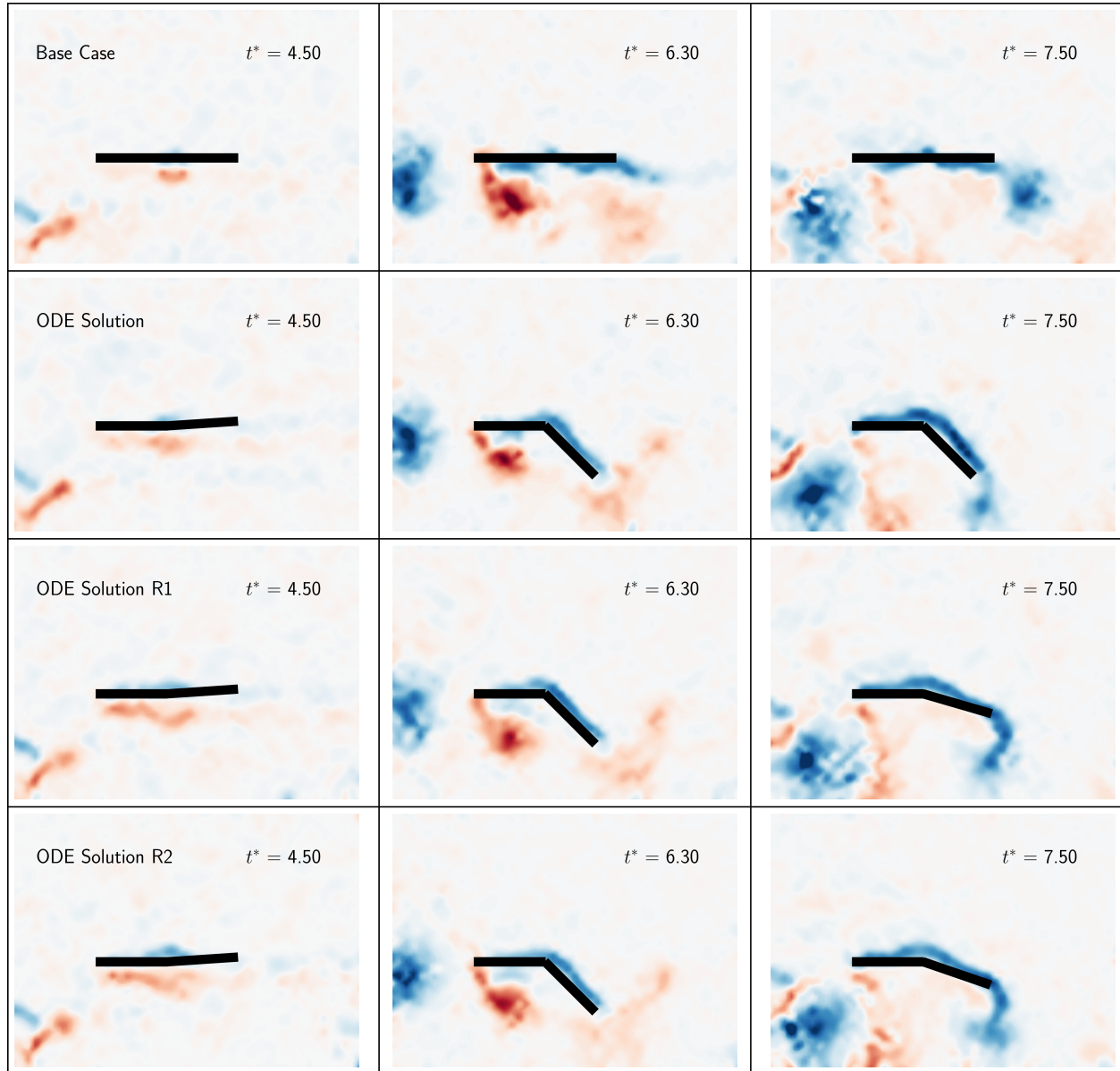


Fig. 14 DPIV images corresponding to the selected instants in no control and controlled experiments.

The DPIV results clearly show that the flow around the leading edge is not affected much by any of the control strategies. This is also evident in the effective angle of attack measurements. A slight flap-up induces positive vorticity layer at the lower surface of the model and is sufficient to overcome the initial small positive lift peak at the beginning of gust generator motion, namely at $t^* = 4.5$. The mitigation in the later instants is achieved by the new presence of the negative vorticity layer on the upper surface of the wing model and the change in the shedding of the negative trailing edge vortex.

IV. Conclusion

This study proposes and experimentally demonstrates the use of effective angle of attack measurements taken from upstream of a NACA0012 wing for the mitigation of gust-induced loads by feed-forwarding the measurements to actuate a trailing edge flap to exploit the temporal gap between the measurement and the force development to make gust mitigation experiments more applicable to flight testing on MAVs.

A series of experiments have been performed in the air for a NACA0012 wing encountering a continuous vortex gust in the wake of an upstream circular cylinder. A force-based control was attempted but was not successful. The loading on the wing has been measured simultaneously with the effective angle of attack using a multi-hole pitot probe and a correlation between the effective angle of attack and lift was observed with a coherent phase difference. A feed-forward control strategy was attempted by using this phase difference between the measurement and force generation. However, due to the inertial forces generated by the motion of the trailing edge flap and the servo itself, the aerodynamic forces acting on the wing during the controlled experiments could not be isolated. Nevertheless, it was shown that the magnitude of the oscillations caused by the inertial forces is in the same order of magnitude as the aerodynamic ones, suggesting that the control strategy may have been effective.

Another series of follow-up experiments have been performed in the water channel for a flat plate wing encountering a discrete vortex gust generated with another flat plate upstream of the test model as a result of a half-turn rotation. Another control strategy that takes the non-circulatory forces into account was attempted. Since it is challenging to perform real-time angle of attack measurements in water, several experiments were conducted to show the applicability of the effective angle of attack for gust mitigation. Later on, the DPIV images were used to extract the angle of attack signal and compare it with the lift signal, which shows a significant correlation.

Following the extraction, obtained force data was used to generate a flap deflection profile to mitigate the effects of the gust which takes the virtual camber and added mass effects into account with an ordinary differential equation. Even though this solution provided a significant improvement in the initial behavior of the force profile, the inability of the model to capture the resulting flow field's effects led to undesired forces of the original magnitude with just a 15% reduction in the negative peak while amplifying the positive peak by nearly 11%. These effects were smoothed with the introduction of a linear ramp down to the flap profile, resulting in a way more effective alleviation of the loads with a 70% reduction in the negative peak and a 29% reduction in the positive peak. With a final addition of a negative ramp-down profile, an overall reduction of 74% was observed for the negative peak while an 82% reduction was observed for the positive peak.

In addition to these experiments, a proportional-derivative force-feedback controller was implemented as well. This controller reduced the negative peak by 38% but effectively did nothing for the positive peak. The lack of performance for this controller can be explained by the inherent time lag the system possesses. By the time the voltage signal coming out of the sensor is read by the DAQ, multiplied with the calibration matrix and went into the real-time Butterworth filter, the root cause of the force generation already clears the trailing edge, dissipating in the chaotic wake.

Appendix

Appendix A: Validation of the ODE Solution

To make sure the solution of the ordinary differential equation solution is accurate, the obtained results were tested by comparing them to the original data.

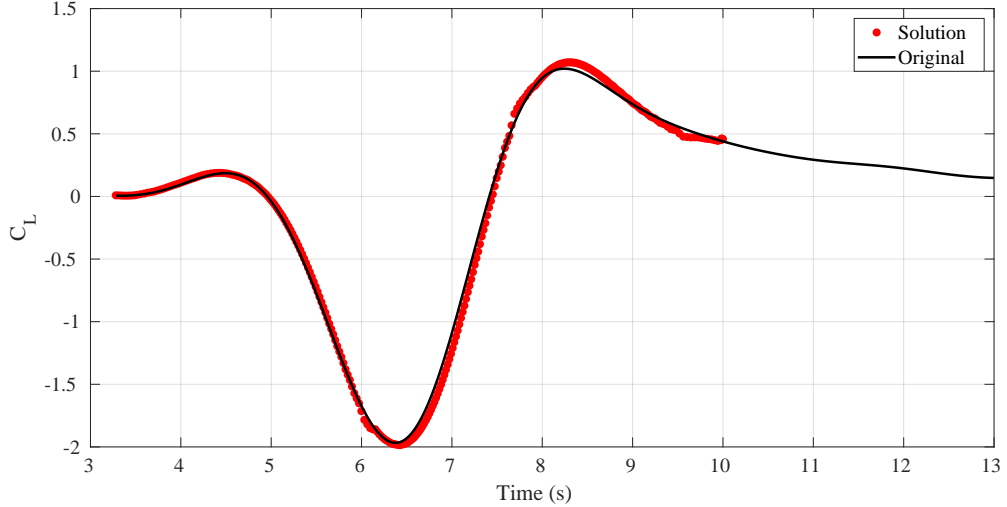


Fig. 15 ODE solution validation.

Appendix B: Flap Reference Tracking

A series of DPIV images has been investigated to verify that the flap deflections commanded to the servo are actually being followed. This process has been performed with the help of a brief Python script that makes use of the Hough transform from OpenCV library [20] which extracts the angular deflection of the flap from the images. Even though the method does not capture each of the edges perfectly, it generally finds more than one edge corresponding to the actual edges of the wing. In order to overcome this issue, all of the found lines are averaged. Then, lines with a z-score greater than 2 are eliminated. After this operation, the mean angle of the remaining lines is stored in the respective position in the array for the corresponding image. Sample images for the method can be seen in Figure 16.

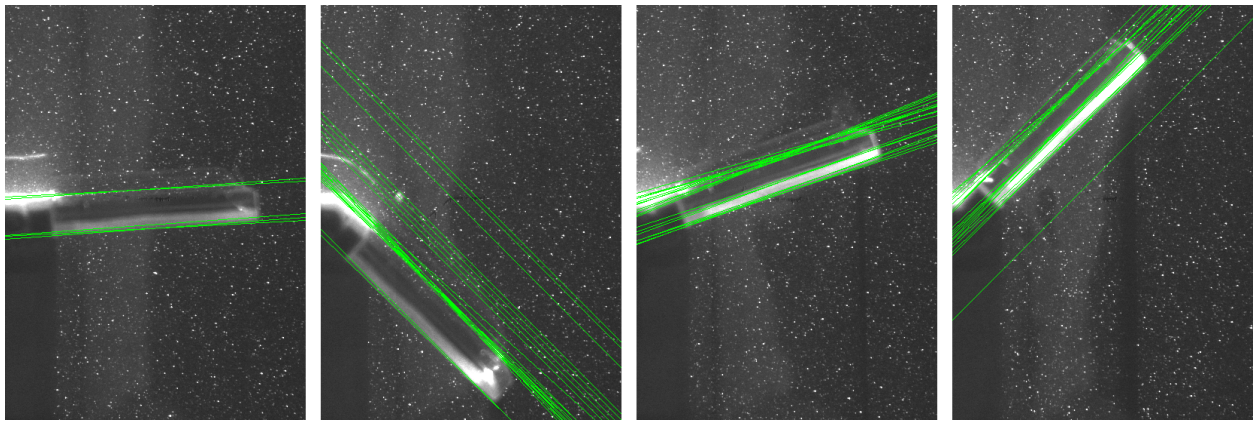


Fig. 16 Flap angle extraction from DPIV images.

The method is applied to the ODE solution case presented in Figure 10. Even though some outliers exist in the data, it can be seen in Figure 17 that the results are in good agreement with each other.

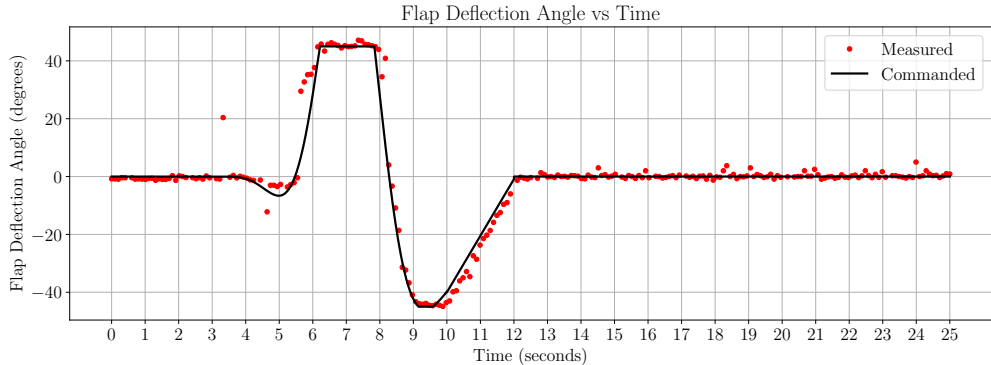


Fig. 17 Flap deflection angle commanded compared to measured from the DPIV images.

Acknowledgments

During the course of experimentation in Toulouse, Efe Egemen SEN was funded by ENAC - Airbus - Sopra Steria Drones and UTM Research Chair.

References

- [1] Barrado, C., Boyero, M., Bruculeri, L., Ferrara, G., Hately, A., Hullah, P., Martin-Marrero, D., Pastor, E., Rushton, A., and Volkert, A., “U-Space Concept of Operations: a key enabler for opening airspace to emerging Low-Altitude operations,” *Aerospace*, Vol. 7, No. 3, 2020, p. 24. <https://doi.org/10.3390/aerospace7030024>, URL <https://doi.org/10.3390/aerospace7030024>.
- [2] Watkins, S., Milbank, J., Loxton, B., and Melbourne, W., “Atmospheric winds and their implications for microair vehicles,” *AIAA Journal*, Vol. 44, No. 11, 2006, pp. 2591–2600. <https://doi.org/10.2514/1.22670>, URL <https://doi.org/10.2514/1.22670>.
- [3] Zarovy, S., Costello, M., Mehta, A., Gremillion, G., Miller, D. S., Ranganathan, B. N., Humbert, J. S., and Samuel, P., “Experimental study of gust effects on micro air vehicles,” *AIAA Atmospheric Flight Mechanics Conference*, 2010. <https://doi.org/10.2514/6.2010-7818>, URL <https://doi.org/10.2514/6.2010-7818>.
- [4] Jones, A. R., Cetiner, O., and Smith, M. J., “Physics and Modeling of large flow disturbances: Discrete gust encounters for modern air vehicles,” *Annual Review of Fluid Mechanics*, Vol. 54, No. 1, 2022, pp. 469–493. <https://doi.org/10.1146/annurev-fluid-031621-085520>, URL <https://doi.org/10.1146/annurev-fluid-031621-085520>.
- [5] Jones, A. R., and Cetiner, O., “Overview of unsteady aerodynamic response of rigid wings in gust encounters,” *AIAA Journal*, Vol. 59, No. 2, 2021, pp. 731–736. <https://doi.org/10.2514/1.j059602>, URL <https://doi.org/10.2514/1.j059602>.
- [6] Chowdhury, J., and Ringuette, M., “Effect of a rotating and swept wingtip on streamwise gust alleviation,” *AIAA Journal*, Vol. 59, No. 3, 2021, pp. 800–811. <https://doi.org/10.2514/1.j059690>, URL <https://doi.org/10.2514/1.j059690>.
- [7] Angulo, I. A., and Babinsky, H., “Negating gust effects by actively pitching a wing,” *AIAA Scitech 2020 Forum*, 2020. <https://doi.org/10.2514/6.2020-1057>, URL <https://doi.org/10.2514/6.2020-1057>.
- [8] Andreu-Angulo, I., and Babinsky, H., “Controlling upwards and downwards gust loads on aerofoils by pitching,” *Exp Fluids*, Vol. 64, No. 129, 2023, pp. 786–799.
- [9] Acar, E., “Use of LESP (Leading Edge Suction Parameter) and Effective Angle of Attack Measurements for Gust Mitigation,” *M.Sc. Thesis*, ITU 2023.
- [10] Andreu-Angulo, I., and Babinsky, H., “Mitigation of airfoil gust loads through pitch,” *AIAA Journal*, Vol. 60, No. 9, 2022, pp. 5273–5285.

- [11] Sedky, G., Gementzopoulos, A., Andreu-Angulo, I., Lagor, F. D., and Jones, A. R., “Physics of gust response mitigation in open-loop pitching manoeuvres,” *Journal of Fluid Mechanics*, Vol. 944, 2022, p. A38.
- [12] Biler, H., Sedky, G., Jones, A. R., Saritas, M., and Cetiner, O., “Experimental investigation of transverse and vortex gust encounters at low Reynolds numbers,” *AIAA Journal*, Vol. 59, No. 3, 2021, pp. 786–799.
- [13] Son, O., and Cetiner, O., “Three-Dimensionality Effects due to Change in the Aspect Ratio for the Flow around an Impulsively Pitching Flat Plate,” *Journal of Aerospace Engineering*, Vol. 30, No. 5, 2017. [https://doi.org/10.1061/\(asce\)as.1943-5525.0000765](https://doi.org/10.1061/(asce)as.1943-5525.0000765), URL [https://doi.org/10.1061/\(asce\)as.1943-5525.0000765](https://doi.org/10.1061/(asce)as.1943-5525.0000765).
- [14] Bronz, M., Gavrilović, N., Drouin, A., Hattenberger, G., and Moschetta, J., “Flight testing of dynamic soaring Part-1 : Leeward Inclined Circle Trajectory,” *AIAA Scitech 2021 Forum*, 2021. <https://doi.org/10.2514/6.2021-1527>, URL <https://doi.org/10.2514/6.2021-1527>.
- [15] Engin, K., Aydin, E., Zaloglu, B., Fenercioglu, I., and Cetiner, O., “Large scale spanwise periodic vortex gusts or single spanwise vortex impinging on a rectangular wing,” *2018 Fluid Dynamics Conference*, 2018, p. 3086.
- [16] Babu, A. V. S., Medina, A., Rockwood, M., Bryant, M., and Gopalarathnam, A., “Theoretical and experimental investigation of an unsteady airfoil in the presence of external flow disturbances,” *Journal of Fluid Mechanics*, Vol. 921, 2021. <https://doi.org/10.1017/jfm.2021.484>, URL <https://doi.org/10.1017/jfm.2021.484>.
- [17] Soy, K., Tugan, E., Acar, E., and Cetiner-Yildirim, O. N., “Experimental investigation of discrete to continuous vortex gust encounters,” *AIAA SCITECH 2023 Forum*, 2023. <https://doi.org/10.2514/6.2023-1621>, URL <https://doi.org/10.2514/6.2023-1621>.
- [18] Babinsky, H., Stevens, R. J., Jones, A. R., Bernal, L. P., and Ol, M., “Low order modelling of lift forces for unsteady pitching and surging wings,” *54th AIAA Aerospace Sciences Meeting*, 2016. <https://doi.org/10.2514/6.2016-0290>, URL <https://doi.org/10.2514/6.2016-0290>.
- [19] Leishman, J. G., *Principles of Helicopter Aerodynamics*, Cambridge University Press, 2002.
- [20] Bradski, G., “The OpenCV Library,” *Dr. Dobb’s Journal of Software Tools*, 2000.